

Ultrafast lasers and solids in highly excited states: results of hydrodynamics and molecular dynamics simulations

This content has been downloaded from IOPscience. Please scroll down to see the full text.

2014 J. Phys.: Conf. Ser. 510 012041

(<http://iopscience.iop.org/1742-6596/510/1/012041>)

View [the table of contents for this issue](#), or go to the [journal homepage](#) for more

Download details:

IP Address: 79.139.219.36

This content was downloaded on 14/06/2014 at 11:10

Please note that [terms and conditions apply](#).

Ultrafast lasers and solids in highly excited states: results of hydrodynamics and molecular dynamics simulations

Nail A. Inogamov¹, Vasily V. Zhakhovsky², Viktor A. Khokhlov¹,
Sergey I. Ashitkov², Yusuf N. Emirov³, Konstantin V.
Khichshenko², Anatoly Ya. Faenov^{2,4}, Tatiana A. Pikuz⁴, Masahiko
Ishino⁴, Masaki Kando⁴, Nobory Hasegawa⁴, Masaharu Nishikino⁴,
Pavel S. Komarov², Brian J. Demaske⁶, Mikhail B. Agranat²,
Sergey I. Anisimov¹, Tetsuya Kawachi⁴, Ivan I. Oleynik⁷

¹ Landau Institute for Theoretical Physics, Russian Academy of Sciences, Russian Federation

² Joint Institute for High Temperatures of Russian Academy of Sciences, Russian Federation

³ Advance Materials Research Institute, Florida International University, USA

⁴ Quantum Beam Science Directorate, Japan Atomic Energy Agency, Japan

⁵ University of Florida, USA

⁶ Department of Physics, University of South Florida, USA

E-mail: nailinogamov@gmail.com (N. Inogamov)

Abstract. Action of ultrafast optical and X-ray lasers on metals is considered. It is known that under certain conditions surface structures appear as result of irradiation. Generation of nano-structures is usually associated with excitation of surface plasmons. But often structures do not have forms of ripples, and their spacial scales are order of magnitude less than optical wavelength. In the paper full description of surface nano-structures is given for the case of single shot laser action onto well polished boundaries. Plasmon effects are insignificant for this case and also for X-ray pulses. It is shown that structures are formed after laser illumination in a process of mechanical spallation of ultrathin surface layer of molten metal. Spallation is accompanied by a strong foaming of melt, breaking of foam, and freezing of foam remnants. Those remnants form chaotic nano-structures observed in experiments.

1. Introduction

Lasers with ultrashort pulse (durations τ_L from ~ 10 fs to few ps) have a wide range of technological and bio-medical applications. There are applications where only ultrafast lasers solve problem. E.g., those lasers are irreplaceable in the studies of elastic-plastic [1, 2, 3] or polymorphic transformations near atomistic limit, and in studies of picosecond [4] chemical reactions (detonation under action of very high and very short mechanical load). Physics of energy transfer from photons to material heating and motion is not trivial. In metals we have to consider a two-temperature (2T) state [5] to understand origin of subsequent phenomena. Density functional theory (DFT) is necessary to approximate quantum electronic properties used in 2T thermodynamic and transport calculations. Hierarchy of scales from fs to ns have to be taken into account to follow formation of surface structures directly from a 2T stage.



In the paper we compare ultrafast actions of optical and X-ray lasers. Previously people have attributed structure formation solely to an interference between incident electromagnetic wave and surface plasmons [6, 7] (ripples, spacing between ripples ~ 1 μm). Another insight starts from a paper [8]; it was shown that thermomechanical effects (nucleation and spallation) are responsible for structure formation after small number of shots N of optical lasers $h\nu \sim 1$ eV onto well polished surfaces (the case of random structures, spatial scales $\sim d_T$ - thermal depth). Plasmons are absent in case of X-rays. Therefore thermomechanics is responsible for structure formation under action of ultrashort X-ray pulse at any number of shots. In future a hybrid approach including both a plasmon interference and a thermomechanics will be developed. It will allow to describe universally the cases with an arbitrary set of parameters N , $h\nu$, and incident fluence. In this paper we limit ourselves to a thermomechanical ablation.

The mentioned spatiotemporal hierarchy is shown in Fig. 1. Electron thermal wave emits compression wave "compr" at a transonic stage. At a 2T stage a trajectory of the thermal wave corresponds to the bottom-right edge of the hatched region in Fig. 1(a). Compression wave runs away into the bulk, while a thermal layer remains near boundary. Gradually compression wave breaks and a shock wave appears. This event takes place at the right side relative to an area shown in Fig. 1. It isn't shown. Slightly above ablation threshold F_{abl} the nucleation begins in a narrow layer near the point where a reflected acoustic wave intersects with compression wave running to the left, see Fig. 1 (a). Two lines going up from the intersection point of acoustic characteristics in Fig. 1 (a) present the left and right edges of a layer filled by two-phase mixture. Appearance of mixture strongly decreases dynamic and thermal contacts between the edges.

Significantly above an ablation threshold F_{abl} a wide nucleation zone 2-3 appears, see Fig. 1 (b). Above evaporation threshold F_{ev} the condensed layer 1-2 (spallation plate) disappears [9]. In the interval of fluences $F_{abl} < F < F_{ev}$ the layer 1-2 consists from hot liquid. The points a, m, and f in Fig. 1 (b) correspond to an instants

(a) When the last characteristics of compression wave leaves the thermal layer.

(m) Maximum penetration of melting front. In this point melting changes to solidification.

(f) Total freezing of molten layer between the curves 3 and 4 in Fig. 1 (b), see Section 3 below. Molten metal in the layer 1-2 remains hot for a long time after freezing of the right edge.

Liquid in the point f freezes during $\sim \text{ns}$ time interval. Near the point f the random surface structures form if breaking of foam in vicinity of the edge 3 in Fig. 1 (b) lasts longer than solidification of melt between the lines 3-4, see Section 3 below. We see that a process of formation of surface structures covers many orders of magnitudes - 7 orders if duration of pulse is 100 fs.

Short pulse laser ablation is better understood in case of optical lasers. In this case on metals the ablation threshold F_{abl} is 2-3 times higher than a melting threshold F_m . Therefore if we are interested to study active motions¹ we have enough energy to melt a solid fast. In this case nucleation shown in Fig. 1 takes place in liquid. We can regard the bottom boundary of a 2T region and curve 4 in Fig. 1 (b) as a trajectory of a melting zone. Melting zone is filled by solid-liquid mixture. This zone is wide at a 2T stage, and becomes much more narrow at a 1T stage. Ablation by X-ray lasers has similarities and differences with optical lasers, we will discuss them below. Here let's mention few features. In metals the radiation energy of optical lasers $h\nu \sim 1$ eV is absorbed in intraband and interband transitions in the upper electronic shells. This energy almost entirely transfers to conduction electrons. Then 2T state appears since electrons are excited during shorter time interval τ_L than they will cool later t_{eq} . During the 2T stage the electrons gently transfer energy to ions: $h\nu \rightarrow T_e \rightarrow T_i$. This transfer proceeds through small steps of numerous e-i collisions. During the interval t_{eq} the electrons are hot, and thermal energy spreads to a spatially significant depth d_T many times larger than a skin depth.

¹ This needs $F > F_{abl}$, more exactly $F > F_{nucl}$, where F_{nucl} is a nucleation threshold. The F_{nucl} is 1-10% below F_{abl} .

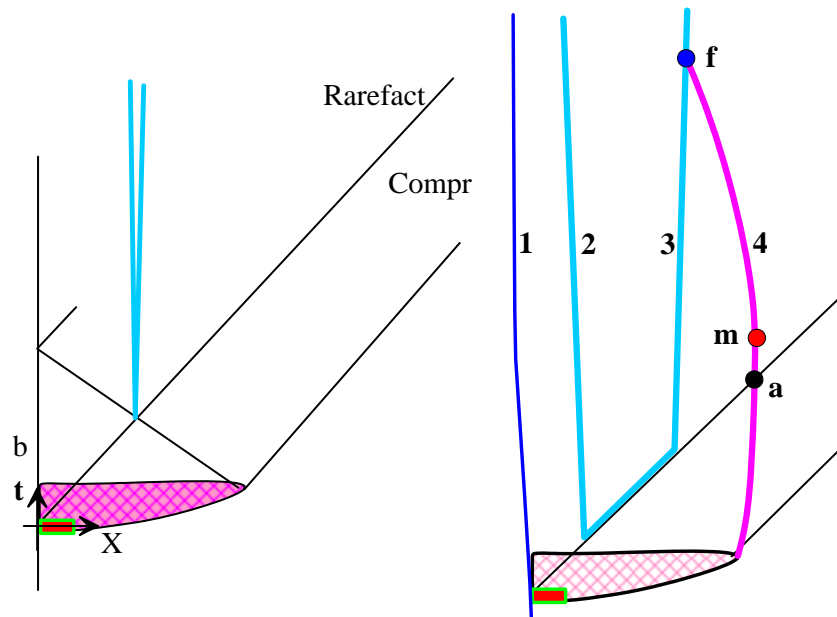


Figure 1. The x, t diagram of sequence of processes initiated by ultrashort pulse. Time is reckoned from an instant when pulse intensity at a vacuum-target boundary "b" achieves maximum. Distance along a normal x to the boundary is reckoned from initial (prior to pulse) position of a boundary. (a) The red rectangular is an absorption region $\tau_L \times \delta$, where δ is a skin depth for optical irradiation and an attenuation depth for X-rays. The rectangular where electrons were strongly excited is placed inside 2T region where system gradually returns to electron-ion equilibrium $T_e = T_i$. This is the hatched region with spatiotemporal dimensions $t_{eq} \times d_T$, where t_{eq} , d_T are duration of temperature equilibration and thickness of thermal layer created during 2T stage, resp. Velocity of heat penetration is higher than speed of sound c_s at a 2T stage. This velocity sharply drops down below c_s during transition from 2T to 1T (one-temperature) stage. Compression nonlinear acoustic wave "compr" separates from a thermal layer during this transit. (b) The lines 1, 2-3, and 4 correspond to a vacuum boundary, edges of a mixture layer, and to melting-recrystallization front, resp.

This increases F_{abl} since density of energy per unit volume necessary to overcome material strength weakly depends on value of d_T , see paper [10] where has been shown that $F_{abl} \propto d_{film}$ for thin films $d_{film} < d_T$.

In case of hard photons situation in metals is different. Very significant part of energy $h\nu$ directly transfers to ion energy [11]. Absorption of energy $h\nu$ by ion ionizes electron. This electron escapes from the ion thus changing charge of this ion. Ion with changed charge and its ion surrounding "immediately" (if we compare the transition period to an ion time scale which is an inverse Debye frequency ~ 0.1 ps) increase potential energy of their interaction ("immediately" means during the time of escape ~ 1 fs of an ionized electron from the ion). Fraction of this potential energy during the ion time scale transits to kinetic energy of ion motions. This rises internal energy and pressure of ion subsystem [11]. Such direct transfer $h\nu \rightarrow T_i$ decreases electron energy at a 2T stage. Thus decreasing importance of thermal layer created by electron heat conduction in metal at a "standard" 2T stage. Instead a thermal layer of directly heated ions appears. Its thickness is defined by attenuation depth d_{att} of hard photons. The depth d_{att} may be significantly thinner than a thermal depth d_T linked with electron conduction. Expansion of heat from the layer d_{att} is restricted since holes are sitting at deep electron shells (therefore tunneling probability is low) while mobility of ions typically is small.

Also additional heating of electron subsystem from ions from attenuation depth is small since temperature of ions is small in comparison with electron temperatures. Therefore spreading of ion energy from the depth d_{att} through usual electron heat conduction is small. At comparable energies stored in electron subsystem and directly in ions the energy density per unit of volume may be significantly higher in the layer d_{att} . This will decrease ablation threshold on absorbed energy and ablation depth at a threshold in case of hard photons in comparison with optical lasers.

Let's mention that a thermal depth in dielectrics should be of the order of the attenuation depth d_{att} since electron heat conduction is small. Let's also mention that it is difficult to study a range of intermediate absorbed energies in optical ablation of dielectrics because they are transparent and absorption begins only after optical breakdown when matter is too hot. While in the X-ray case the depth d_{att} is fixed and small, matter is non-transparent and absorbing, and we can continuously create all states from below melting threshold F_m and up to F_{abl} and higher varying fluence F . Then regimes with foaming of molten dielectrics should exist. But it is difficult to freeze those foams because conduction cooling is slow.

2. Hydrodynamic expansion driven by electron pressure

2T states obeys 2T equation of state (EOS). This is a three dimensional EOS T_e, T_i, ρ . Pressure cold curves $p(\rho, T_e = 0, T_i = 0)$ for nickel together with a low temperature 1T isotherm $T = 0.529$ kK are shown in Fig. 2 (a). DFT cold curves satisfactory agree with each other and with the curves obtained from a wide-range EOS. DFT and EOS agree up to the point where pressure sharply increases to a value $p = 0$ on the EOS curve. This is a point of minimum of the (EOS, $T = 0$) curve in Fig. 2 (a). This point corresponds to the point in Fig. 3 (a) where continuation of spinodal, liquidus, and solidus touch the $T = 0$ axis. Fig. 2 (b) illustrates how excitation of electron subsystem increases total pressure. This increase is obvious since we see that pressure $p(\rho, T_i = 0, T_e)$ at equilibrium density $\rho = 8.9$ g/cc rises from zero at $T_e = 0$ to ≈ 75 GPa at $T_e = 2.5$ eV. Similar DFT calculations of pressures of 2T crystals with cold ions (fixed in their lattice positions) was performed in works [12] (W), [13] (Ni), and [14] (Al,W).

Phase diagram of 1T EOS [15, 16] is shown in Fig. 3 (a). Two-phase region outlined by binodal consists from subregions of metastability and absolute instability separated by spinodal. Solidus and liquidus are prolonged through binodal in Fig. 3 (a). Solidus and liquidus are boundaries of solid-liquid mixture. It was found [16] that in most of metals liquidus intersects spinodal before the spinodal achieves the zero temperature limit. Aluminum is an example where liquidus and spinodal both independently reach the zero temperature limit. A zone of solid-liquid mixture can not exist if one of its boundary disappears. Therefore it is hypothesized that the spinodal achieves zero temperature at smaller degree of stretching (along a continuation of solidus in Fig. 3 a). Therefore a minimum of a cold curve taken from the 1T EOS in Fig. 2 (a) is achieved significantly earlier than the minimum of the pressure well obtained by DFT or taken from [17].

Our molecular dynamics (MD) operates with embedded atom model (EAM) interatomic potentials describing many-body interactions. Our EAM potentials for Al and Au were developed in paper [19], EAM potential for nickel has been obtained in [20]. Electron temperature dependent EAM have been constructed based on DFT results obtained on a dense grid of (ρ, T_e) points. Electron pressure corresponding to this EAM is shown in Fig. 3 (b). 2T hydrodynamics code is based on a 2T EOS. In this 2T EOS the total pressure is presented as $p(\rho, T_e, T_i) = p_i(\rho, T_i) + p_e(\rho, T_e)$, where p_e is found from equation $p_e(\rho, T_e, T_i = 0) = p(\rho, T_e, T_i = 0) - p(\rho, T_e = 0, T_i = 0)$ and it is supposed that $p_e(\rho, T_e, T_i)$ weakly depends on T_i , here p is total pressure. In 2T EOS the ion pressure $p_i(\rho, T_i)$ is taken as pressure $p(\rho, T)$ from 1T EOS (without electronic Fermi type addition used in wide-range EOS) with substitution of T_i in place of temperature T . In 2T EOS the electron pressure is

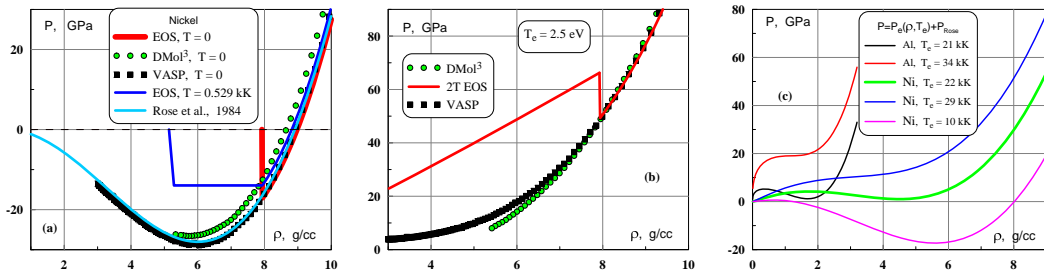


Figure 2. (a) Cold curves from density functional theory (DFT), wide-range 1T EOS [15, 16], and from analytical approximation [17]. DMol³ (accelrys materials-studio) and VASP [18] packages are used for DFT calculations. (b) Dependence of total pressure of system on density at fixed ion $T_i = 0$ and electron $T_e = 2.5$ eV temperatures. (c) Isotherms of total pressure $p(\rho)$ for $T_i = 0$, $T_e = \text{fixed}$. They are calculated as a sum $p = p_e(\rho, T_e) + p_{Rose}(\rho)$, where p_e is electron pressure and p_{Rose} is taken from [17]. We see that there is an interval $0 < T_e < T_{min}$ where the profiles p have minimums; $T_{min} = 32$ kK (2.7 eV) for Al and 26 kK (2.25 eV) for Ni. The minimum degenerates into an inflection point at $T_e \rightarrow T_{min} - 0$. There is also important subinterval $T_+ < T_e < T_{min}$ where p in the minimum is positive; $T_+ = 20.5$ kK (1.8 eV) for Al and 21 kK (1.8 eV) for Ni. Isothermal ($T_e = \text{const}$) expansion flow has an equilibrium point on a right branch of dependence $p(\rho, T_e)$ if $0 < T_e < T_+$. Situation with a rarefaction jumps becomes possible in case $T_+ < T_e < T_{min}$, see text for explanations.

approximated as [13] (ρ in g/cc, T_e in K, approximation is based on DFT calculations)

$$p_e(\rho, T_e) = 1.1(\rho/8.91)^{1.1} K S (K + S)^{-1}, \quad K = 1077 T_e^2 / 2, \quad S = 1.275 \cdot 10^5 T_e^{1.3}. \quad (1)$$

This approximation for $T_e = 2.5$ eV is presented as a curve "appr" in Fig. 3 (b).

There is an important difference between EAM and 2T EOS. The 2T EOS is based on 1T EOS. Approximation of metastable region in the 1T EOS shown in Figs. 2 and 3 (a) is influenced by measurements done at rather large spatiotemporal scales $\sim \text{mm}$ and μs . Therefore the left slope of a "well" in a cold pressure profile "2T EOS" in Fig. 2 (a) is steep. In atomistic situation this slope should be more smooth, it should be more close to DFT data and to the curve "Rose et al." [17] as it is shown in Fig. 2 (c). The main question is: are there a well at a pressure profile when a whole profile is above the axis $p = 0$? Of course, there is a well in a case of a steep left slope at any electron temperature. Fig. 2 (c) demonstrates, first, that there are cases with a smooth well and, second, that there are cases with positive total pressure in the minimum of a well. Why this question is significant for us? We are searching for regime of *gaseous* rarefaction under action of dominating electron pressure. In this case the metal outflow is composed from atoms with excited electrons since matter remains in 2T state. Then a possibility to obtain macroscopic hydrodynamic *source of excited atoms* appears.

There are two scenarios. In the first of them the sharp rarefaction jump (RFJ) appears. Its existence is obvious from Figs. 3 (c) and 4. In the second scenarios there are or less productive² 2T evaporation from a boundary of 2T metal, or continuous flow without a rarefaction jump. Our 2T-HD code presents flows with a vacuum boundary if surface temperature T_e is below the limit T_+ described in a caption to Fig. 2 (c). And in 2T-HD we always have a rarefaction jump above this limit since in a case of a well with steep left slope (see Fig. 2 a) we have a feature in the form of a well on the dependence $p(\rho)$ shown in Fig. 2 (b) at any temperature $T_e > T_+$; because the temperature $T_{min} = \infty$ for this case with steep slope. Corresponding

² In comp. with RFJ in the sense of amount of excited atoms.

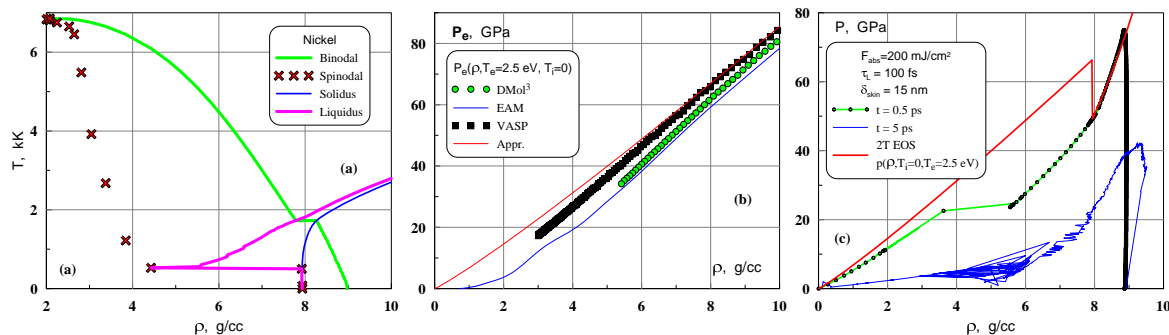


Figure 3. (a) The ρ, T plane of a 1T EOS. The binodal bounds a two-phase region where equilibrium vapor contacts with condensed phase. A strip of a melting zone is continued inside a metastable region. Cold curves shown in Fig. 2 (a) go along the horizontal axis $T = 0$. (b) DFT data and their approximation with help of EAM and simple analytic approximation "appr." (1) taken from [13]. Electron pressure p_e is defined from equation $p(\rho, T_e, T_i = 0) = p(\rho, T_e = 0, T_i = 0) + p_e(\rho, T_e, T_i = 0)$. (c) 2T EOS isothermal curve from Fig. 2 (b) and two instant profiles obtained by 2T hydrodynamics (2T-HD) code in case of nickel. Instant spatial distributions $\rho(x, t_{fix})$ and $p(x, t_{fix})$ are presented here as a parametric plot. In metal far from vacuum boundary we have $\rho \rightarrow \rho_0 = 8.9$ g/cc, $p \rightarrow 0$. Pressure increases when we approach to the boundary and after that decreases in the rarefaction flow. The first part of the rarefaction decrease of p follows 2T EOS isothermal curve at the distributions corresponding to an early instants.

hypothetical flow is shown in Fig. 4. There are four main parts of this flow. They corresponds to profile $t = 0.5$ ps shown in Fig. 3 (c). The first part is an isochoric rise of pressure from initial value $p = 0$. It locates before the point where velocity changes sign in Fig. 4 (b) and where the decreases of pressure and density begin in Fig. 4 (c). In the second part the matter of nickel expands along the right slope of a well in Fig. 2 (b). The third part corresponds to a jump. It connects two points: one in the minimum of a well and other point is outside the jump. The fourth part corresponds to a freely expanding flow outside the jump. During the 2T stage the 2-3 monoatomic layers pass the jump for the conditions of pulse shown in Figs. 3(c) and 4.

Let us emphasize that as was said above we are interested here in a rarefaction flow going from a surface and on early 2T stage. We will not consider stretching of matter as result of deceleration of boundary, creation of tensile stress, nucleation, and spallation. Indeed, early rarefaction covers a small part of a heated layer d_T . At this stage $t \ll t_s = d_T/c_s$ and deceleration isn't significant. Spallation under influence of electron pressure has been considered in papers [21, 22]. see also papers [23, 24] where pressure p_e was presented as a blast force.

We run MD simulations with EAM potential to check microscopic picture connected with expansion under action of electron pressure. Special EAM potential of nickel including electron temperature effects has been developed. This development is based on DFT calculations shown in Figs. 2 (a,b) and 3 (b). Resulting pressure dependencies $p(\rho, T_e = \text{fixed}, T_i = \text{fixed})$ (isotherms) are shown in Figs. 2 (c) and 3 (b). Figs. 2 (c) and 3 (b) present total pressure and electron contribution to total pressure, resp. Dependencies for Al are obtained in a Fermi model for conduction electrons, while dependencies for Ni are based on a set of DFT simulations. There are two approximations of pressure p_e shown in Fig. 3 (b) both based on the DFT simulations. One is a simple approximation (1) taken from [13]. It is shown as the curve "appr." in Fig. 3

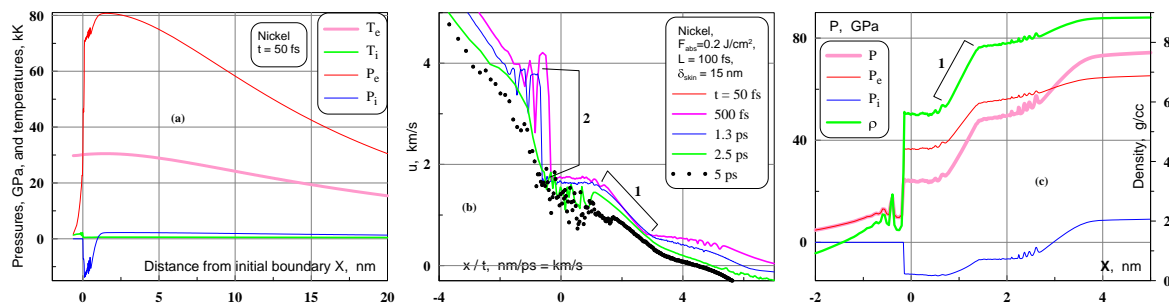


Figure 4. (a) Electron temperature and pressure dominate at an early 2T stage. Their distributions are shown at the end of laser pulse $t = 50$ fs; duration of pulse is $\tau_L = 100$ fs, see caption in Fig. 3 (c) where parameters of a laser pulse are given. Time is reckoned from a maximum in time of a laser pulse. Let us emphasize creation of significant tensile ion stress. This is a result of expansion stretching driven by huge electron pressure. (b) Velocity jump corresponding to RFJ is marked by digits 1 and 2. The head of a rarefaction wave runs with velocity $\approx 5 - 7$ km/s. At the end of a 2T stage this velocity drops to 4-5 km/s - speed of sound in Ni. (c) Pressure and density jumps, comp. with Figs. 4 (b), 3 (c) and 2 (b).

(b). Other is a curve "EAM" in Fig. 3 (b). It is calculated from the EAM potential. EAM potential is presented as a multi-parameters rational function minimizing deviations of pressure and energy surfaces from the dense set of the data points on a ρ, T_e plane obtained thanks to DFT. Simplex approach based on n -dimensional geometrical figures (program ameba) is used for optimization of n (few tens) parameters of the rational function.

The curves "appr." and "EAM" in Fig. 3 (b) are slightly different. Therefore their ρ, p -isotherms also differ. The ρ, p -isotherms corresponding to the approximation (1) for Ni and the curve "appr." in Fig. 3 (b) are shown in Fig. 2 (c). Isotherms for Ni are obtained by summing the approximation (1) and expression for cold pressure from the paper [17]. This family of isotherms has an interval $T_+ < T_e < T_{min}$ smaller than the same interval for Al. In degrees of softness of the pressure well on the isotherm there are 2T EOS (the most stiff well), Al in Fig. 2 (c), Ni in Fig. 2 (c), and Ni based on the EAM potential. The most soft well corresponds to the case of Ni described by EAM potential (a curve "EAM" in Fig. 3 (b)). It has the shortest interval (T_+, T_{min}) , the minimum of a well goes far away in direction of small densities at the axis of ρ before the minimum passes into halfspace $p > 0$.

The RFJ may appear in the interval (T_+, T_{min}) . Our set of electron temperatures T_e where MD simulations have been performed covers a range from 0 to 3 eV with a step 0.5 eV. We see that the value 2.5 eV is below the interval while the value 3 eV is above the interval. A shallow well means weak cohesion energy. A shallow well forms under stretching action of electron pressure. Metal with small cohesion is more volatile - evaporation proceeds more intensively at lower ion temperatures. Why the pressure well and the interval (T_+, T_{min}) are important are discussed in Fig. 5 (a). Initial state of Ni $\rho = 8.9$ g/cc, $p = 0$ is shown as the point 1 in Fig. 5 (a). Isochoric heating rises pressure to a value corresponding to temperature T_e - arrow 2. After that expansion begins. It decreases pressure along the arrow 3 in Fig. 5 (a). There are three cases in Fig. 5 (a) corresponding to different temperatures T_e . In the first case temperatures T_e belongs to the interval $(0, T_+)$ - there is a minimum and it is below the axis $p = 0$. Then expansion stops in the point 4 when positive electron pressure and negative ion pressure balance each other.

The most interesting is the second case where temperature T_e belongs to the interval (T_+, T_{min}) . The isotherm for this case is shown in Fig. 5 (a) as a blue curve with a minimum

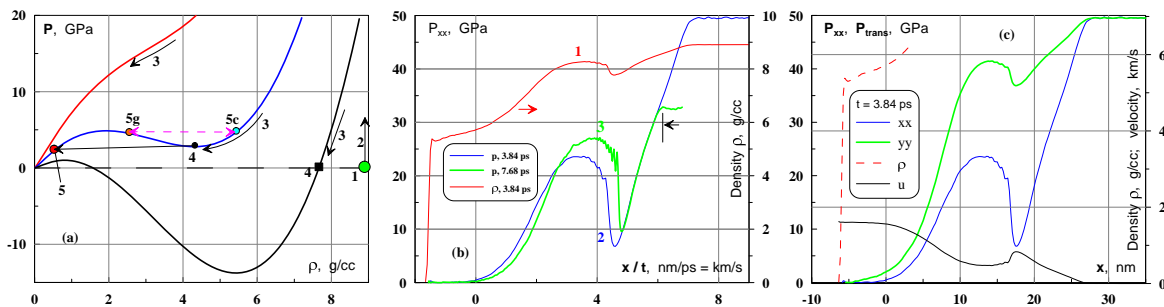


Figure 5. (a) Nickel ρ, p -isotherms taken from Fig. 2 (c) for other set of temperatures $T_e = 2.9, 2$, and 1.1 eV. Dynamics of isothermal expansion depends on the particular isotherm along which matter expands. There are three qualitatively different ways of expansion depending on value T_e . These ways are shown here, see text for explanations. (b) Expansion of a fcc single nickel crystal 100 nm thick along direction 111 . The left side of an expansion flow is shown. Point $x = 0$ is placed at the initial position of the left boundary of a film. Electron temperature $T_e \equiv 2$ eV distribution is homogeneous across the film. We suppose that values of T_e is conserved in material particles during their motions because we consider an early stage. The left side expansion flow is self-similar $\rho(x, t) \rightarrow \rho(x/t)$ until arrival of the right side rarefaction wave. Approaching of the right wave is marked by the black arrow. (c) Unloading of transverse stress and liberation of transverse elastic energy. We see that transverse stress decays much slower than longitudinal stress during elastic uniaxial stretching. Therefore significant potential energy remains in transverse stresses. While liberation of longitudinal elastic energy accelerates matter at a first part of rarefaction. Drop of density on a density profile marks the vacuum-nickel boundary.

above the axis $p = 0$. A material particle near a vacuum boundary starts from the point 1, rises pressure along the arrow 2, begins to expand along the arrow 3, and arrives to the minimum 4. After that it has to expand further since pressure in the minimum 4 is higher than vacuum pressure. There are two ways to expand. In the first way the expansion proceeds along $4 \rightarrow (5_g, 5_c)$ - the condensed media decays into mixture of low and high density phases 5_g and 5_c due to acoustic instability, see Fig. 5 (a). In the other way from the minimum 4 is a rarefaction jump $4 \rightarrow 5$ decreasing pressure and density and increasing velocity in a style shown in Fig. 4 (b,c). It seems that the RFJ will exist in the case of a soft well shown in Fig. 5 (a) as it exists in a case of a well with a steep left slope. At last the high temperature state in Fig. 5 (a) freely expands as a gas along the path 1-2-3.

MD simulations performed with EAM with short or absent interval (T_+, T_{min}) are shown in Fig. 5, 6. We have began MD studies to understand a microscopic picture accompanying intriguing phenomenon of a RFJ - rarefaction shock. But instead the MD results shed light to another surprising phenomenon - the two-stage rarefaction when longitudinal stress release is followed by a spatially distant release of transverse stress. Longitudinal unloading is simply caused by expansion into vacuum, while the transverse release runs in direction from the vacuum-metal boundary into bulk. The transverse release propagates as a wave against an expansion flow. Thus lattice contribution manifests itself through this two-stage release. We must take into account that crystal survives a short period of time under conditions of heating from excited electrons. It will be interesting to consider an expansion of a 2T molten metal film in future MD simulations.

In Fig. 5 (b) expansion of a solid film under action of pressure p_e overcoming atomic cohesion is shown. Profiles for two time instants are shown against self-similar axis x/t . We

see that simple rarefaction profiles coincide. While the remarkable knoll is accelerated to the right, comp. longitudinal stress profiles 2 and 3. This knoll presents the right edge of a plastic wave propagating to the right side along the rarefaction wave. Propagation of plastic wave is supported by release of elastic energy in the space interval between the plastic front and the $p = 0$ layer near a vacuum boundary. Release of elastic energy is powerful enough to decrease expansion velocity, see Fig. 5 (c), and prevents drop of density - density even increases, see Fig. 5 (b). Fig. 5 (c) demonstrates two-step expansion. This is similar to the case described in papers [25, 26]. In the first step the matter accelerates under gradient of a longitudinal stress. During this acceleration the transverse elastic energy transforms into kinetic energy of expansion. At the first step longitudinal stress drops down much more than transverse stress. Transversely loaded state is unstable. In the second step the plastic transformations releases potential accumulated in transverse directions. This energy unloading send compression wave in both directions: downstream and upstream. The upstream wave as was said decelerates velocity of expansion and even rises density (!), see Fig. 5 (b). While the downstream part additionally accelerates nickel in direction to vacuum, see Fig. 5 (c) with a two-step velocity profile.

3. Freezing of nanostructures

Above the early 2T stage has been considered. Later equilibration of temperatures of electron and ion subsystem takes place, see Fig. 1. Typically duration of equilibration t_{eq} is shorter than acoustic time scale $t_s = d_T/c_s$. Thus hydrodynamic motions on the scales $\sim d_T$ and $\sim t_s$ take place in 1T metal. Below ablation threshold F_{abl} the back characteristics of compression wave running to the right and the back characteristics of compression wave running to the left intersects in the middle of a heated layer d_T , see Fig. 1 (a). The strip "Compr" in Fig. 1 (a) corresponds to the right compression wave. The strip "Rarefact" is filled with a reflected wave $p < 0$ running to the right. It forms during reflection of the left compression wave from a vacuum boundary. This reflection changes sign of stress. Shift of a boundary stops after reflection of the back characteristics of the left compression wave. Contact between the fluxes of the right running characteristics of the compression and tensile waves "Compr" and "Rarefact" is filled by a fan of characteristics outcoming from the small vicinity of the $x = 0, t = 0$ point. This fan isn't shown in Figs. 1. Spatiotemporal width of the fan gradually increases during its propagation. This process gradually decreases a slope of a pressure profile in the contact zone between the waves "Compr" and "Rarefact".

Below an ablation threshold the maximum stretching and tensile stress are achieved in the point of intersection of the back characteristics of the waves "Compr" and "Rarefact" (width of the fan is small at $t \sim t_s$). Therefore at $F = F_{abl}$ the nucleation starts in this point. Nucleation separates continuous metal in to two part. Nucleation zone evolve into a zone with vapor bubbles. They fill an interior between two blue straights in Fig. 1 (a). In papers [8, 27, 28] it was shown that nucleation threshold F_{nucl} is few percents less than ablation threshold F_{abl} . Above ablation threshold the spallation plate separates and flies away from a main body. The spallation plate is a layer between the vacuum boundary and the left blue straight in Fig. 1 (a). In the interval $F_{nucl} < F < F_{abl}$ there are possibility that bubbles in the layer between the two blue straights in Fig. 1 (a) will remain frozen inside solid. This depend on a competition between the hydrodynamic process of shrinking of bubbles and thermal process of cooling and freezing [28]. The shrinking and bubbles collapses dominate at a final temporal part of cavitation when resistance to stretching overcomes inertia of matter accelerated at an initial expansion stage. This shrinking stage exists since we are below ablation threshold. For optical lasers the ablation threshold is few times higher than melting threshold. Therefore there are bubbles and liquid around the bubbles.

Results of large scale MD simulation including very important ingredient - a Monte-Carlo description of an electron thermal transport are presented in Figs. 6. Those calculations were

made for aluminum. The sizes of matter in a computational domain were $500 \times 240 \times 24 \text{ nm}^3$; 172 millions of atoms. Absorbed fluence is 80 mJ/cm^2 , the ratio to ablation threshold is $80/65 = 1.23$.

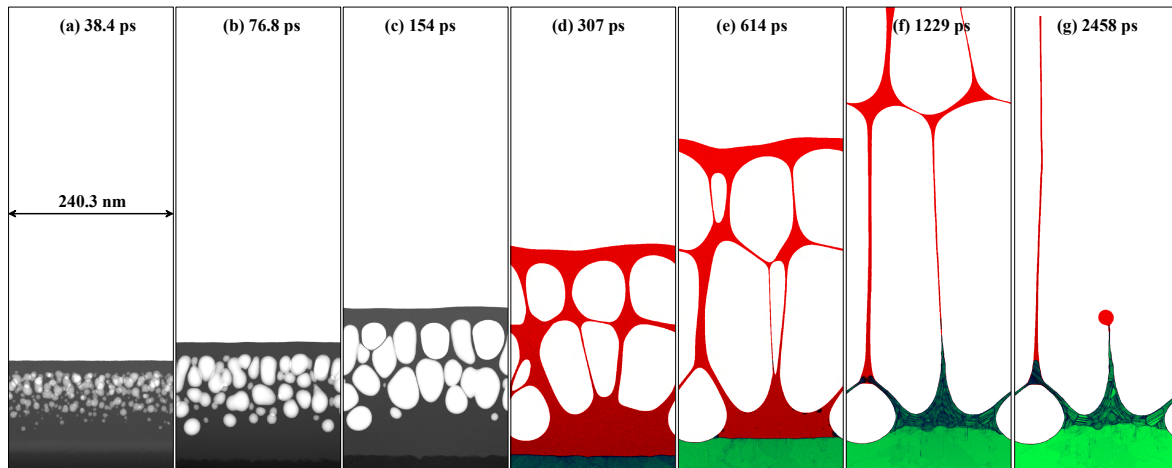


Figure 6. Nucleation, foaming, hydrodynamic decay of strongly stretched foam, appearance of droplets on the tip of jets, and freezing of remnants of broken liquid-vapor foam. Process covers two orders of magnitude in time. MD simulation spans scales from interatomic and up to micron size. Recrystallization front is clearly seen. It gradually approaches the foam region. Three first pictures present density maps. While the four next pictures show evolution of phase composition. The red and green colors correspond to liquid and solid aluminum, resp. Dark green color correspond to a region with ultradense concentration of dislocations. This region forms a "skin" including the frozen surface nanostructures.

Simulation shown in Figs. 6 is important for understanding of phenomena leading to appearance of chaotic structures. The key here is the processes of foam stretching and breaking in interplay with freezing of supercooled liquid. Hydrodynamic motions under action of inertia, tensile stress, and surface tension compete with an equally slow³ solidification up to the end of motion - up to the final stop of motion in a thermally stressed state. A droplet at tip of jet demonstrates an amazing dynamics. Membranes surrounding bubbles in foam are ultimately stretched by inertial expansion up to 2-3 interatomic distances. Membranes break in their thinnest parts. This breaking forms a wall type feature made from a remnant of a membrane. The feature is topped with a droplet at its upper edge. The droplet is a formation elongated along the edge of membrane. It accumulates mass during contraction of broken membrane. It accumulates not only mass but also momentum of this mass. This momentum is created during contraction. Therefore velocity of a droplet differs from velocity of membrane itself. Complicated velocity field appears under action of surface tension and freezing/melting processes taking place in a contact between the liquid droplet and colder solidified membrane. The last picture in the series shown in Fig. 6 shows instant coexistence of liquid red droplet and frozen green jet type membrane. Experimental pictures in Figs. 9-11 below present plenty examples of such membranes, jets, and droplets.

Let us consider the remnant of a membrane attached to the bulk of a target. In Figs. 6 the bulk is located in the bottom of the pictures. As was said, after breaking this remnant begins to contract forming a long droplet along the edge of the broken membrane. In the last picture in Figs. 6 this droplet is elongated in direction perpendicular to the plane of picture.

³ In a final stages they both slow their velocities down to velocities of the order of few tens of m/s.

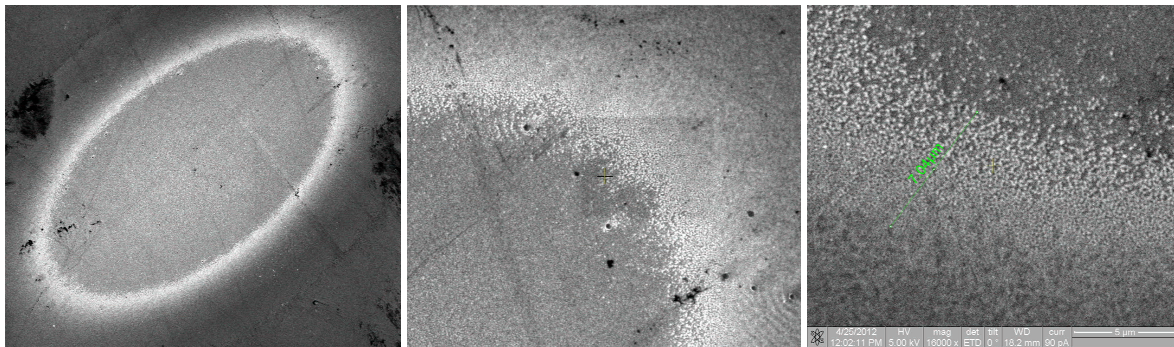


Figure 7. (a) General SEM view of typical crater after irradiation by optical near infrared Cr:forsterite laser. The spot has an elliptical shape since laser beam has been inclined, p -polarization, 45° inclination, wavelength 1240 nm, duration 100 fs. Incident fluence was 480 mJ/cm^2 , absorbed fluence was 220 mJ/cm^2 . Ablation threshold for nickel for these conditions for incident fluence is 320 mJ/cm^2 . The ratio of central to ablation incident fluences is $F_c/F_{abl} = 1.5$. (b) Ring type region of the lateral edge of the crater shown in previous figure. Fluence in this region was near ablation threshold. (c) Enlarged SEM view of the ring region. Length of the green marker going across the lateral ring is $7.04 \text{ } \mu\text{m}$.

In a 3D picture this elongated droplet deforms as a result of inhomogeneity of velocity, stress, and temperature conditions along the droplet. Therefore 3D rounded droplets gradually form from the elongated one. They are clearly seen in the experimental Figures 10 and 11 below. Finally cooling due to pumping of heat from a hot surface layer into bulk totally solidifies liquid masses. Very slow creep continues during subsequent shrinkage of nanocrystallite solid under action of a field of residual stresses. Thus nanostructures appear on an irradiated target surface. Those structures are an interlacement of threads, threads with droplets, and broken and survived undersurface bubbles, see Figs. 9-11. They are mixed with a "skin" from a nanocrystallite solid. Broken and survived undersurface bubbles have narrow entrances going into the undersurface cavities visible in Fig. 10 (c).

Figures 7-9 correspond to ablation of a nickel film deposited onto glass substrate. Similar structures have been obtained in works [29, 30, 31, 32, 33]. The target from Ni has been irradiated by a p -polarized laser pulse from an air side. This is a Cr:forsterite laser. The first harmonics $\lambda = 1240 \text{ nm}$ has been used. Duration of pulse is $\tau_L = 100 \text{ fs}$. Angle of inclination is 45° degrees.

Important quantity is an ablation threshold. Let us give a data corresponding to a nickel target irradiated from an air side. Incident fluence at an ablation threshold is 0.32 J/cm^2 . Of course this value depends on polarization and inclination. While a value of absorbed fluence at an ablation threshold after a single shot is independent on conditions of irradiation (polarization and inclination). Absorbed fluence at an ablation threshold for nickel is 0.14 J/cm^2 . Absorption coefficient A was specially measured. It depends on polarization, inclination, fluence, and duration. Near ablation threshold this coefficient is $A = 0.45$.

Experimental results (Figs. 9, 10) fully confirm our MD modeling of foaming and freezing. In experiments nickel film $\approx 1 \text{ } \mu\text{m}$ thick has been deposited onto glass substrate. Film has been irradiated through air. Chains of single shot craters obtained on a film surface have been analyzed by optical and scanning electron microscopy (SEM). Fig. 7 (a) presents typical crater from such chain of craters.

Figs. 8 demonstrates few steps of FIB sample preparation for TEM (Transmission electron microscopy) - lamella technique. Figs. 9 presents pictures obtained at TEM. They clearly

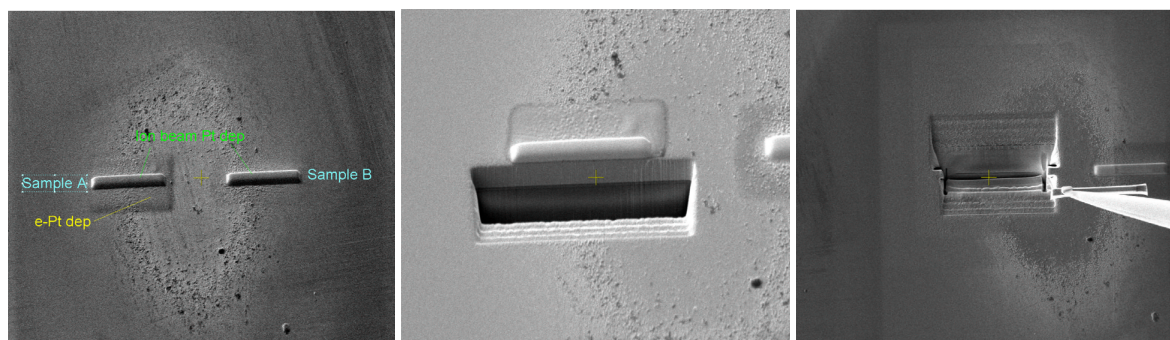


Figure 8. (a) Two protective Pt layers was deposited across a crater ring for preparation of two TEM samples. The left "Sample A" contains two protective Pt layers: 1st - electron stimulated Pt deposition (the square area marked by "e-Pt dep") to avoid Pt penetration into the Ni layer; and 2nd rectangular ion beam stimulated Pt deposition. The right region ("Sample B") has only ion beam Pt deposition with Pt penetration depth up to 50 nm into the nickel layer. (b) Milling of nickel from one side as the first step of future lamella preparation. (c) After two side milling of nickel the lamella has been welded to the nanomanipulator needle and lift out for transportation to TEM sample holder.

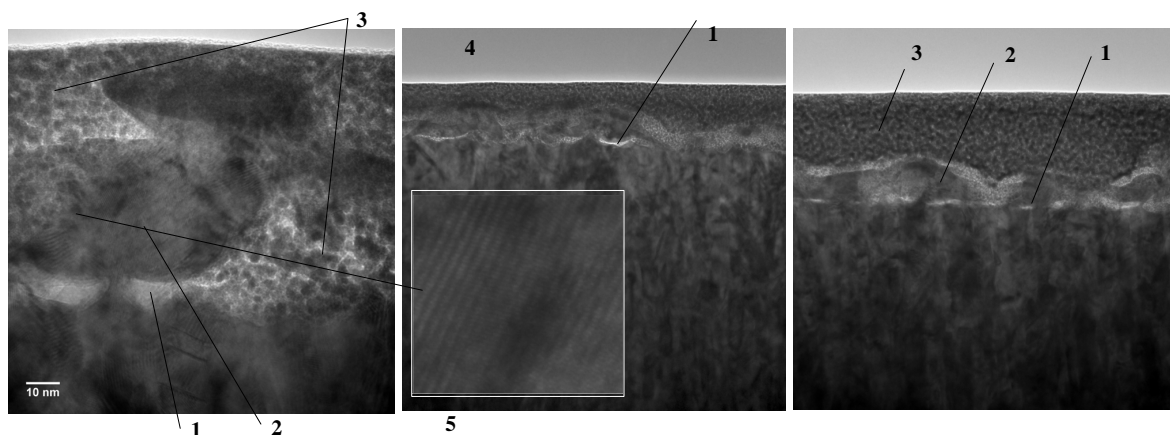


Figure 9. TEM images of irradiated surface of nickel in the region of lateral rings: 1- frozen undersurface bubbles, 2 - frozen jets, 3 - empty spaces filled with the Pt organic, 4 - a vacuum above the organic, 5 - nanocrystallite with visible atomic planes of the lattice. The disk type bubbles have a form of a crescent in a plane perpendicular to a target surface. Horizontal length of the bubble 1 marked in the left panel is 20 nm. The left panel size is $110 \times 110 \text{ nm}^2$; 110 nm is ≈ 2700 pixels.

demonstrate existence of frozen jets and undersurface bubbles in case of nickel. Previously these observations have been made for aluminum [28]. Now their presence is firmly established for transition metal.

SEM images of a crater and structures inside the craters are shown in Figs. 10 for the case of gold. We see that there is no tendency to form ripples even in the case of optical lasers, relatively high fluences, and limited number of shots, see Fig. 10 (c).

The X-ray lasers give us opportunity totally neglect plasmons contribution into formation of surface structures - no ripples at all. The reason is simple - photon frequency is many times higher than plasmon frequencies. Scales of structures enlarge with increasing of number of shots

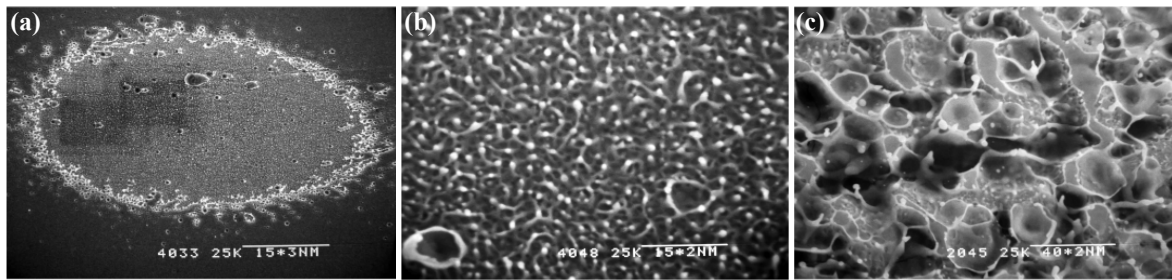


Figure 10. SEM images of surface structures at different magnifications. (a) Crater on a gold surface obtained after a single laser shot with pulse duration $\tau_L = 100$ fs. The scale is $15 \cdot 10^3$ nm = 15 μ m. Relative fluence in the center of elliptical spot is $F_c/F_{abl} = 1.5$. (b) Magnified view of a piece of the crater shown in the previous image. We see a homogeneous field of structures with sparse more large details. The scale is $15 \cdot 10^2$ nm = 1.5 μ m. (c) The small piece of a crater bottom formed by three identical shots into the same spot. Duration is $\tau_L = 100$ fs. Central relative fluence $F_c/F_{abl} = 1.1$ is smaller than in the previous pictures. The scale is $40 \cdot 10^2$ nm = 4 μ m.

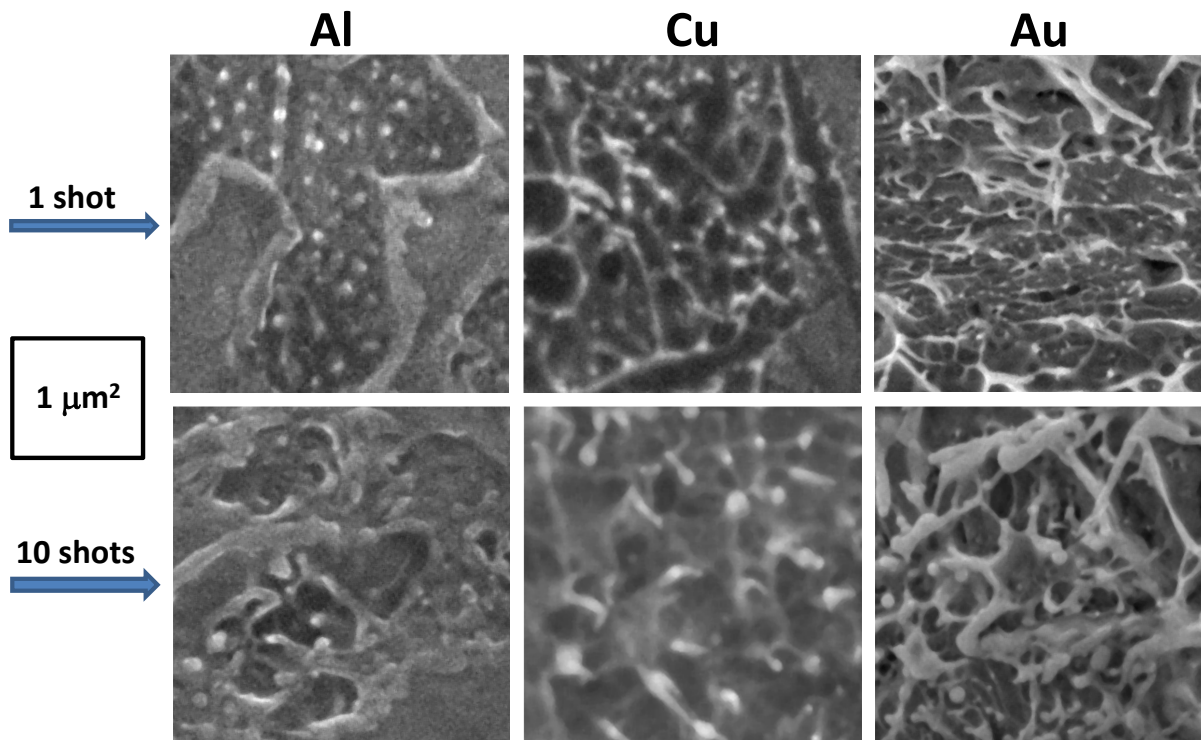


Figure 11. Surface structures formed by short pulse (duration 7 ps) soft X-ray ($h\nu = 90$ eV) laser irradiation. Small pieces from irradiated spots are shown. Area of those spots is ≈ 200 μm^2 . Device is described in papers [34, 35]. Thresholds for ablation are: Al 14 ± 5 mJ/cm²; Cu 16 ± 5 mJ/cm²; Au 21 ± 5 mJ/cm².

N. See examples shown in Fig. 11. This is significant observation.

Ablation threshold is few times lower than in case of optical lasers. This is very important feature of short pulse X-ray ablation. We have to emphasize that we compare *absorbed* fluences (absorbed energy) in optical and X-ray cases necessary to overcome ablation threshold.

Explanation of this fact is linked to physics of 2T stage with excited electrons and to nucleation stage, see Section 1.

Conclusion. Above the early 2T stage in case of metals and optical lasers has been studied. New types of expansion dynamics have been described. Amount of ablated matter (few monoatomic layers) is small. But these atoms are ejected out in an unusual 2T state. This means that atoms remain excited during their separation from main body of a target. Theory and experiments on surface structure formation have been conducted and described. It is important to compare optical and X-ray irradiations. This allows to elucidate plasmons effects connected with interference of incident and surface electromagnetic waves. Surface structures exactly correspond to the picture developed above. The picture is based on phenomena of nucleation, foaming, and freezing of foam remnants appearing as result of mechanical breaking.

Acknowledgments. Authors (MBA, NAI, VVZh, VAKh, SIAsH) acknowledge support from RFBR grant 13-08-01095 A. This work was partly supported by a Grant-in-Aid for Scientific Research (B), No. 25289244, from the Ministry of Education, Culture, Sports, Science, and Technology (MEXT), Japan and by RFBR grants 12-02-00947 A (authors AYaF, TAP). This work was supported by ROSATOM contract H.4x.44.90.13.1111 (authors MBA, NAI, SIAsH).

References

- [1] Agranat M, Anisimov S, Ashitkov S, Zhakhovskii V, Inogamov N, Komarov P, Ovchinnikov A, Fortov V, Khokhlov V and Shepelev V 2010 *JETP Letters* **91** 471–477
- [2] Ashitkov S, Agranat M, Kanel' G, Komarov P and Fortov V 2010 *JETP Letters* **92** 516–520
- [3] Zhakhovskii V V and Inogamov N A 2010 *JETP Lett.* **92** 521–526
- [4] Armstrong M R, Crowhurst J C, Bastea S and Zaug J M 2010 *J. Appl. Phys.* **108** 023511
- [5] Anisimov S, Kapeliovich B and Perel'man T 1974 *Sov. Phys. JETP* **39**(2) 375–377
- [6] Sipe J E, Young J F, Preston J S and van Driel H M 1983 *Phys. Rev. B* **27** 1141–1154 URL <http://link.aps.org/doi/10.1103/PhysRevB.27.1141>
- [7] Akhmanov S A, Emel'yanov V I, Koroteev N I and Seminogov V N 1985 *Sov. Phys. Usp.* **28** 1084–1124 URL <http://iopscience.iop.org/0038-5670/28/12/R02>
- [8] Zhakhovskii V V, Inogamov N A and Nishihara K 2008 *JETP Letters* **87** 423–427
- [9] Inogamov N A, Zhakhovskii V V, Ashitkov S I, Petrov Y V, Agranat M B, Anisimov S I, Nishihara K and Fortov V E 2008 *JETP* **107** 1–19
- [10] Demaske B, Zhakhovsky V, Inogamov N and Oleynik I 2010 *Phys. Rev. B* **82** 064113
- [11] Cherednikov Y, Inogamov N A and Urbassek H M 2013 *Phys. Rev. B* **88** 134109
- [12] Khakshouri S, Alfe D and Duffy D M 2008 *Phys. Rev. B* **78** 224304
- [13] Inogamov N A, Petrov Y V, Zhakhovsky V V, Khokhlov V A, Demaske B J, Ashitkov S I, Khishchenko K V, Migdal K P, Agranat M B, Anisimov S I and Fortov V E 2012 *AIP Conf. Proc.* **1464** 593–608
- [14] Sin'ko G V, Smirnov N A, Ovechkin A A, Levashov P R and Khishchenko K V 2013 *High Energy Density Physics* **9** 309–314
- [15] Bushman A V, Kanel' G I, Ni A L and Fortov V E 1993 *Intense dynamic loading of condensed matter* (Taylor & Francis)
- [16] <http://teos.ficp.ac.ru/rusbank/> URL <http://teos.ficp.ac.ru/rusbank/>
- [17] Rose J H, Smith J R, Guinea F and Ferrante J 1984 *Phys. Rev. B* **29** 2963
- [18] Kresse G and Furthmuller J 1996 *Computational Materials Science* **6** 15–50
- [19] Zhakhovskii V, Inogamov N, Petrov Y, Ashitkov S and Nishihara K 2009 *Applied Surface Science* **255** 9592–9596
- [20] Demaske B J, Zhakhovsky V V, White C T and Oleynik I I 2012 *AIP Conference Proceedings* **1426** 1211–1214
- [21] Starikov S V, Stegailov V V, Norman G E, Fortov V E, Ishino M, Tanaka M, Hasegawa N, Nishikino M, Ohba T, Kaihori T, Ochi E, Imazono T, Kavachi T, Tamotsu S, Pikuz T A, Skobelev I Y and Faenov A Y 2011 *JETP Lett.* **93** 642–647
- [22] Norman G E, Starikov S V, Stegailov V V, Saitov I M and Zhilyaev P A 2013 *Contrib. Plasma Phys.* **53** 129–139
- [23] Gan Y and Chen J K 2010 *Mechanics of Materials* **42** 491–501
- [24] Chen J, Chen W K and Rentzepis P M 2011 *J. Appl. Phys.* **109** 113522 URL <http://dx.doi.org/10.1063/1.3594732>
- [25] Anisimov S, Zhakhovskii V, Inogamov N and et al 2003 *JETP Lett.* **77** 606–610

- [26] Anisimov S I, Zhakhovskii V V, Inogamov N A, Nishihara K and Petrov Y V 2007 *Appl. Surf. Sci.* **253** 6390–6393
- [27] Zhakhovskii V V, Inogamov N A and Nishihara K 2008 *J. Phys.: Conf. Ser.* **112** 042080
- [28] Ashitkov S, Inogamov N, Zhakhovsky V, Emirov Y, Agranat M, Oleinik I, Anisimov S and Fortov V 2012 *JETP Lett.* **95** 176–181
- [29] Vorobyev A Y and Guo C 2011 *J. Appl. Phys.* **110** 043102 [9 pages] URL <http://dx.doi.org/10.1063/1.3620898>
- [30] Ionin A A, Kudryashov S I, Makarov S V, Seleznev L V, Sinitsyn D V, Ligachev A E, Golosov E V and Kolobov Y R 2013 *Laser Phys. Lett.* **10** 056004
- [31] Hashida M, Ikuta Y, Miyasaka Y, Tokita S and Sakabe S 2013 *Appl. Phys. Lett.* **102** 174106
- [32] Savolainen J M, Christensen M S and Balling P 2011 *Phys. Rev. B* **84** 193410
- [33] Gurevich E L 2011 *Phys. Rev. E* **83** 031604 [5 pages] URL <http://link.aps.org/doi/10.1103/PhysRevE.83.031604>
- [34] Ishino M, Faenov A Y, Tanaka M, Hasegawa N, Nishikino M, Tamotsu S, Pikuz T A, Inogamov N A, Zhakhovsky V V, Skobelev I Y, Fortov V E, Khohlov V A, Shepelev V V, Ohba T, Kaihori T, Ochi Y, Imazono T and Kawachi T 2011 *Journal of Applied Physics* **109** 013504
- [35] Ishino M, Faenov A, Tanaka M, Hasegawa N, Nishikino M, Tamotsu S, Pikuz T, Inogamov N, Zhakhovsky V, Skobelev I, Fortov V, Khohlov V, Shepelev V, Ohba T, Kaihori T, Ochi Y, Imazono T and Kawachi T 2012 *AIP Conference Proceedings* **1465** 236–240